PHYSICAL REVIEW E **82**, 031405 (2010)

Phase behavior and structure of colloidal bowl-shaped particles: Simulations

Matthieu Marechal and Marjolein Dijkstra*
Soft Condensed Matter, Debye Institute for NanoMaterials Science, Utrecht University,
Princetonplein 5, 3584 CC Utrecht, The Netherlands

(Received 1 July 2010; published 23 September 2010)

We study the phase behavior of bowl-shaped particles using computer simulations. These particles were found experimentally to form a metastable wormlike fluid phase in which the bowl-shaped particles have a strong tendency to stack on top of each other [M. Marechal *et al.*, Nano Lett. **10**, 1907 (2010)]. In this work, we show that the transition from the low-density fluid to the wormlike phase has an interesting effect on the equation of state. The simulation results also show that the wormlike fluid phase transforms spontaneously into a columnar phase for bowls that are sufficiently deep. Furthermore, we describe the phase behavior as obtained from free energy calculations employing Monte Carlo simulations. The columnar phase is stable for bowl shapes ranging from infinitely thin bowls to surprisingly shallow bowls. Aside from a large region of stability for the columnar phase, the phase diagram features four novel crystal phases and a region where the stable fluid contains wormlike stacks.

DOI: 10.1103/PhysRevE.82.031405 PACS number(s): 82.70.Dd, 64.70.D−, 81.30.Dz

I. INTRODUCTION

The concept of a mesogenic particle in the form of a bowl is relatively old in the molecular liquid crystal community. Such molecules are expected to form a columnar phase, which can be ferroelectric, i.e., a phase with a net electric dipole moment, when the particles possess a permanent dipole moment. Ferroelectric phases have potential applications for optical and electronic devices. In fact, crystalline (as opposed to liquid crystalline) ferroelectrics are already applied in sensors, electromechanical devices and nonvolatile memory [1]. A columnar ferroelectric phase may have the advantage over a crystal, that is grain boundaries and other defects anneal out faster due to the partially fluid nature of the columnar phase. In reality, columnar phases of conventional disklike particles often exhibit many defects, as flat thin disks can diffuse out of a column and columns can split up. The presence of these defects limits their potential use for industrial applications [2]. Fewer defects are expected in a columnar phase of bowl-shaped mesogens, where particles are supposed to be more confined in the lateral directions. A whole variety of bowl-like molecules have already been synthesized and investigated experimentally [3–6]. In addition, buckybowlic molecules, i.e., fragments of C_{60} whose dangling bonds have been saturated with hydrogen atoms, have been shown to crystallize in a columnar fashion [7–11]. However, the number of theoretical studies is very limited as it is difficult to model the complicated particle shape in theory and simulations. In a recent simulation study, the attractive-repulsive Gay-Berne potential generalized to bowl-shaped particles has been used to investigate the stacking of bowl-like mesogens as a function of temperature [2]. The authors reported a nematic phase and a columnar phase. This columnar phase did not exhibit overall ferroelectric order, although polar regions were found. In another very recent simulation study [12] of hard contact lenses (infinitely thin, shallow bowls), a new type of fluid phase was found in which the particles cluster on a spherical surface for bowls which are not too shallow. No columnar phase was found since the focus was on rather shallow bowls at a relatively low densities.

Recently, a procedure has been developed to synthesize bowl-shaped colloidal particles [13]. This method starts with the preparation of highly uniform oil-in-water emulsion droplets. Subsequently, the droplets were used as templates around which a solid shell with tunable thickness is grown. In the next step of the synthesis, the oil in the droplets is dissolved and finally, during drying, the shells collapse into hemispherical double-walled bowls. In addition to these larger, more easily imaged colloids, a whole variety of bowl-shaped nanoparticles and smaller colloids have been synthesized and characterized[14–19], and possible applications of these systems have been put forward. We also note that recently hemispherical particles were synthesized at an air-solution interface [20] and on a substrate [21]. These hemispherical particles are intended to be used as microlense arrays, but they can also serve as a new type of shape-anisotropic colloidal particle.

In our simulations, we model the particles as the solid of revolution of a crescent [see Fig. 1(a)]. The diameter σ of the particle and the thickness D are defined as indicated in

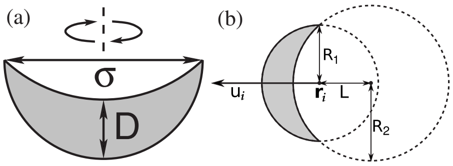

FIG. 1. (a) The theoretical model of the colloidal bowl is the solid of revolution of a crescent around the axis indicated by the dashed line. The thickness of the double-walled bowl is denoted by D and the diameter of the bowl by σ. (b) The bowls are defined using two spheres of radii R_1 and R_2, that are a distance of L apart. The direction vector, $\mathbf{u}_i$ and the reference point of the particle, $\mathbf{r}_i$, (the dot in the center of the smaller sphere) are indicated.

---

*m.dijkstra1@uu.nl

Fig. 1(a). We define the shape parameter of the bowls by a reduced thickness D/σ, such that the model reduces to infinitely thin hemispherical surfaces for $D/\sigma=0$ and to solid hemispheres for $D/\sigma=0.5$. The advantages of this simple model is that it interpolates continuously between an infinitely thin bowl and a hemispherical solid particle (the two colloidal model systems, which we discussed above), and that we can derive an algorithm that tests for overlaps between pairs of bowls, which is a prerequisite for Monte Carlo (MC) simulations of hard-core systems.

In a recent combined experimental and simulation study (for which we performed the simulations), the phase behavior of repulsive bowl-shaped colloids was investigated [22]. The colloids were shown to form a wormlike fluid phase, in which the particles form long curved stacks running in random directions. By comparing the distribution of stack lengths, the simulation model was shown to describe the colloidal particles well. No evidence of columnar ordering was found in the experiments and in simulations of bowls with corresponding deepness, which was explained by the glassy behavior of the particles preventing rearrangements. The phase behavior of the model particles is expected to also describe other repulsive bowl-shaped particles well, provided that the dimensions of the simulation particle are chosen such that the diameter of a stack and the interparticle distance in the stack are the same as for the particles to be modeled.

In this work, we expand the simulation results on the hard bowl-shaped particles. First, we elaborate on the model for the collapsed shells; the overlap algorithm is described in the appendix. Also, the (free energy) methods are explained in more detail than in Ref. [22]. In the results section, we study the properties of the isotropic phase. We investigate the nature and the location of the transition between the homogeneous fluid phase and the fluid phase that contains the wormlike stacks. Furthermore, we show the packing diagram and the phase diagram with a tentative homogeneous-to-wormlike fluid transition line. In the last section we summarize and discuss the results.

II. METHODS

A. Model

We describe the model that we use to represent the bowls in more detail. Consider a sphere with a radius R_1 at the origin and a second sphere with radius $R_2>R_1$ at position $-L\mathbf{u}_i$, where $\mathbf{u}_i$ is the unit vector denoting the orientation of the bowl and $L>0$. The bowl is represented by that part of the sphere with radius R_1 that has no overlap with the larger sphere, see Fig. 1(b). We have chosen the values for L and R_2 such that the bowls are hemispherical (see Appendix for explicit expressions for L and R_2). We define the thickness of the bowls by $D=L-(R_2-R_1)$, such that the model reduces to the surface of a hemisphere for $D=0$ and to a solid hemisphere for $D=R_1$. The volume of the particle is $\frac{\pi}{4}D(\sigma^2-D\sigma+\frac{2}{3}D^2)$, where $\sigma\equiv 2R_1$ is our unit of length. The algorithm to determine overlap between our bowls is described in the appendix.

B. Fluid phase

We employ standard *NPT* MC simulations to obtain the equation of state (EOS) for the fluid phase. In addition, we obtain the compressibility by measuring the fluctuations in the volume:

$$\frac{\langle V^2\rangle-\langle V\rangle^2}{\langle V\rangle}=\frac{k_BT}{\rho}\left(\frac{\partial\rho}{\partial P}\right)_T, \tag{1}$$

where $\rho=N/V$ is the number density and the derivative of the pressure is taken at constant temperature is denoted by the subscript T. We determine the free energy at density ρ_1 by integrating the EOS from reference density ρ_0 to ρ_1,

$$\frac{F(\rho_1)}{N}=\mu(\rho_0)-\frac{P(\rho_0)}{\rho_0}+\int_{\rho_0}^{\rho_1}\frac{P(\rho)}{\rho^2}d\rho, \tag{2}$$

where the chemical potential $\mu(\rho_0)$ is determined using the Widom particle insertion method [23], and $P(\rho_0)$ is determined by a local fit to the EOS.

To investigate the structure of the fluid phase, we measure the positional correlation function [24],

$$g_c(z)=\frac{1}{N\rho A_{\text{col}}}\left\langle\sum_{i=1}^{N}\sum_{j=1}^{N_{\text{col}}(i)}\delta(\mathbf{r}_{ij}\cdot\mathbf{u}_i-z)\right\rangle, \tag{3}$$

where the sum over j runs over $N_{\text{col}}(i)$ particles in a column of radius $\sigma/2$ with orientation u_i centered around particle i, and where the area of the column is denoted by $A_{\text{col}}=\pi\sigma^2/4$. At sufficiently high pressure the particles stack on top of each other to form disordered wormlike piles which resemble the stacks observed in the experiments [22]. As the stacks have a strong tendency to buckle, we cannot use $g_c(z)$ to determine the length of the stacks. We therefore determine the stack size distribution using a cluster criterion. Particle i and j belong to the same cluster if

$$|\mathbf{r}_{ij}+(\zeta D/2+\sigma/4)(\mathbf{u}_j-\mathbf{u}_i)|<\sigma/2 \quad \text{and} \quad \mathbf{u}_i\cdot\mathbf{u}_j>0, \tag{4}$$

and where the first condition has to be satisfied for $\zeta=-1$, 0, or 1 and $\mathbf{r}_{ij}=\mathbf{r}_j-\mathbf{r}_i$, with $\mathbf{r}_i$ denoting the center of the sphere with radius R_1 of particle i, see Fig. 1(b). If both conditions are satisfied, particle j is just above ($\zeta=1$) or below ($\zeta=-1$) particle i in the stack, or, when the stack is curved, particle j can be next to particle i ($\zeta=0$). We now define the cluster distribution as the fraction of particles that belongs to a cluster of size n: $\mathcal{P}_{\text{stack}}(n)\equiv nN_n/N$, where N_n is the number of clusters of size n. We checked that the cluster size distribution does not depend sensitively to the choice of parameters in Eq. (4).

C. Columnar phases

We also perform *NPT* Monte Carlo simulations of the columnar phase using a rectangular simulation box with varying box lengths in order to relax the interparticle distance in the z direction, along the columns, independently from the lattice constant in the horizontal direction. The difference between the free energy of the columnar phase at a certain density and the free energy of the fluid phase at a lower density is determined using a thermodynamic integration technique [25]. We apply a potential which couples a particle to its column,

$$\Phi_{\mathrm{hex}}(\mathbf{r}^N,\lambda) = \lambda \sum_{i=1}^{N} \cos(2\pi N_x x_i/L_x)\sin(\pi N_y y_i/L_y), \tag{5}$$

where x_i and y_i are the x and y components, respectively, of $\mathbf{r}_i$, N_α is the number of columns in the α direction and L_α is the size of the box in the α direction. In our simulations, we calculate Eq. (5) while fixing the center of mass. To do so efficiently, we first calculate all four combinations

$$\lambda \sum_{i=1}^{N} \mathrm{trig}_1(2\pi N_x x_i/L_x)\mathrm{trig}_2(\pi N_y y_i/L_y) \tag{6}$$

for $\mathrm{trig}_1=\cos,\sin$ and $\mathrm{trig}_2=\cos,\sin$. The change in these four expressions upon displacement of a single particle while keeping the center of mass fixed can be expressed in terms of single particle properties and the previous values of the expressions by using some basic trigonometry. In this way, $\Phi_{\mathrm{hex}}(\mathbf{r}^N,\lambda)$, which is Eq. (6) for $\mathrm{trig}_1=\cos$ and $\mathrm{trig}_2=\sin$, can be calculated without performing the full summation over all particles in Eq. (6) every time we displace a particle. Unfortunately, this calculation requires the evaluation of many more trigonometric functions than the simple expression (5), but the extra computation time is negligible compared to the overlap check.

In addition to this positional potential, we also constrain the direction of the particle, using the potential

$$\Phi_{\mathrm{ang}}(\mathbf{u}^N,\lambda) = \lambda' \sum_{i=1}^{N} u_{i,z}, \tag{7}$$

where we used $\lambda'=0.1\lambda$ and where $u_{i,z}$ is the z component of $\mathbf{u}_i$. The thermodynamic integration path from the columnar phase to the fluid is as follows: we start from the columnar phase at a certain density ρ_2. Subsequently, we slowly turn on the two potentials, i.e., we increase λ from 0 to $\lambda_{\max}$. Next, we integrate the equation of state to go from ρ_2 to ρ_1, while keeping $\lambda=\lambda_{\max}$ fixed. During this step the columnar phase will only be stable below the coexistence density, if $\lambda_{\max}$ is sufficiently high. We find that $\lambda_{\max}=20k_BT$ suffices to guarantee stability of the columnar phase. Finally, fixing the density ρ_1, we gradually turn off the potentials, while integrating over λ from $\lambda_{\max}$ to 0. During this last step, the columnar phase melts continuously, provided that the density ρ_1 is low enough and that λ is high enough to prevent melting during the density integration step. The resulting free energy difference between the columnar phase and fluid phase is given by

$$\begin{aligned} F_{\mathrm{col}}(\rho_2) - F_{\mathrm{fluid}}(\rho_1) = {}& \int_0^{\lambda_{\max}} d\lambda \langle \Phi_{\mathrm{hex}}(\mathbf{r}^N,\lambda) + \Phi_{\mathrm{ang}}(\mathbf{u}^N,\lambda)\rangle/\lambda\big|_{\rho=\rho_1} + \int_{\rho_1}^{\rho_2} d\rho \left.\frac{NP(\rho)}{\rho^2}\right|_{\lambda=\lambda_{\max}} \\ & - \int_0^{\lambda_{\max}} d\lambda \langle \Phi_{\mathrm{hex}}(\mathbf{r}^N,\lambda) + \Phi_{\mathrm{ang}}(\mathbf{u}^N,\lambda)\rangle/\lambda\big|_{\rho=\rho_2} \end{aligned} \tag{8}$$

The positional potential [Eq. (5)] is designed to stabilize a hexagonal array of columns, but, strictly speaking, it does not have the hexagonal symmetry of the columnar phase, since it is not invariant under a 60° rotation of the whole system around a lattice position. However, we find that replacing Eq. (5) by a positional potential that does have this symmetry, does not have a significant effect on the free energy difference.

A second type of columnar phase can be constructed by flipping half of the bowls. In this way we obtain alternating vertical sheets (i.e., rows of columns) of bowls that point upward and sheets of bowls that point downward, we will refer to this phase as the inverted columnar phase. We calculate the free energy of this phase using the method described above, with the modification that the angular potential now reads,

$$\Phi_{\mathrm{ang}}(\mathbf{u}^N,\lambda) = \lambda' \sum_{i} u_{i,z}^2. \tag{9}$$

This potential could also have been used for the noninverted columnar phase, and we have found that the result of the free energy integration for the columnar phase is the same whether we use Eqs. (9) or (7).

D. Crystals

1. Packing

As the crystal phases of the bowls are not known *a priori*, we developed a pressure annealing method to obtain the possible crystal phases [26], which we named after the thermal annealing technique [27] commonly used to find energy minima. Many methods to find possible crystal structures exist, although the bulk of these methods minimize the energy (or enthalpy) of the system [27], which is the most important term in the free energy for atomic systems at room temperature. However, entropy plays a large role in many soft matter systems and the corresponding hard-core simulation models. Furthermore, many of these methods start with an initial guess for the crystal structure (for instance from experimental x-ray studies [28]) and allow the box shape and/or positions and orientations of the molecules in the box to adjust using MC or molecular dynamics (MD) simulations. Phase transitions between different crystal structures can be observed in such simulations [29,30]. However, we feel it is safer to start with a random initial configuration to avoid biasing toward a specific crystal structure. Methods that do perform such an unbiased search, typically use some form of pressure [31] or temperature [32] annealing during the simulations, which breaks the (detailed) balance condition (that is, these methods cause a deviation from the Boltzmann distribution). If the only objective is to find the closest packed state as in Ref. [31], there is no real reason to obey the balance condition. However, if the objective is to find stable crystal structures, to use a simulation which samples configuration spacer according to the Boltzmann distribution, such as regular MC or MD, is an advantage. If, in addition, a system of only a few particles is studied, such that all possible states can be sampled even at relatively high pressure, the most stable state is certain to be found. A second consequence of using such a small system is the likelihood of large fluctuations allowing the system to visit states that are metastable for small system sizes, but which might be stable for the larger systems of interest. Similar ideas were formulated in an independent and earlier study [32] of possible ice structures using MD at fixed volume and box shape combined with energy minimization with respect to both the coordinates and the box shape parameters (this combination breaks the balance condition). Our algorithm for finding crystal structures obeys the (detailed) balance condition and has been tested on a large number of soft matter systems [26].

Fully variable box shape *NPT* Monte Carlo simulations, which were first developed by Najafabadi *et al.* [30], were performed on systems of only two to six particles. By construction, the final configuration of such a simulation is a crystal, where the unit cell is the simulation box. One cycle of such a simulation consists of the following steps: We start at a pressure of $10k_BT/\sigma^3$. Subsequently, we run a series of simulations, where the pressure increases by a factor of ten each run: $P\sigma^3/k_BT=10,100,\ldots,10^6$. At the highest pressure ($10^6k_BT/\sigma^3$) we measure the density and angular order parameters, $S_1\equiv\|\langle\mathbf{u}_i\rangle\|$ and $S_2\equiv\lambda_2$, where λ_2 is the highest eigenvalue of the matrix whose components are $Q_{\alpha_\beta}=\frac{3}{2}\langle u_{i\alpha}u_{i\beta}\rangle-\frac{1}{2}\delta_{\alpha\beta}$, where $\alpha,\beta=x,y,z$. We store the density if it is the highest density found so far for these values of S_1 and S_2. We ran 1000 of such cycles for each aspect ratio, which is enough to visit each crystal phase multiple times. After completing the simulations, we tried to determine the lattice parameters of the resulting crystal by hand. Although this last step is not necessary, it is convenient to have analytical expressions for the lattice vectors and the density. The pressure annealing runs were performed for $D/\sigma=0.1,0.15,\ldots,0.5$. For many of the crystals, we were not able to find analytical expressions for the lattice parameters. For these crystals, we obtain the densities of the close packed crystals for intermittent values of D by averaging the density in single simulation runs at a pressure of $10^6k_BT/\sigma^3$. The initial configurations for the value of D of interest were obtained from the final configurations of the pressure annealing simulations for another value of D by one of the following two methods, depending on whether we needed to decrease or increase D: When decreasing L no overlaps are created so the final configuration of the simulation for the previous value of L can be used as initial configuration. On the other hand, increasing L results in an overlap, which is removed by scaling the system uniformly. Subsequently, the pressure is stepwise increased from $1000k_BT/\sigma^3$ to $10^6k_BT/\sigma^3$, by multiplying by 10 each step.

2. Free energies

We calculate the free energy of the various crystal phases by thermodynamic integration using the Einstein crystal as a reference state [33]. The Einstein integration scheme that we employ here is similar to the one that was used to calculate the free energies of crystals of dumbbells in Ref. [34]. We briefly sketch the integration scheme here and discuss the modifications that we applied. We couple both the positions and the direction of the particles with a coupling strength λ, such that for $\lambda\to\infty$, the particles are in a perfect crystalline configuration. First, we integrate $\partial F/\partial\lambda$ over λ from zero to a large but finite value for λ. Subsequently we replace the hard-core particle-particle interaction potential by a soft interaction, where we can tune the softness of the potential by the interaction strength γ. We integrate over $\partial F/\partial\gamma$ from a system with essentially hard-core interaction (high $\gamma=\gamma_{\max}$), to an ideal Einstein crystal ($\gamma=0$). Some minor alterations to the scheme of Ref. [34] were introduced, which were necessary, because of the different shape of the particle. For the coupling of the orientation of bowl i, i.e., $\mathbf{u}_i$, to an aligning field, we have to take into account that the bowls have no up down symmetry, while the dumbbells are symmetric under $\mathbf{u}_i\to-\mathbf{u}_i$. The potential energy function that achieves the usual harmonic coupling of the particles to their lattice positions, as well as the new angular coupling, reads

$$\beta U(\mathbf{r}^N,\mathbf{u}^N;\lambda)=\lambda\sum_{i=1}^{N}(\mathbf{r}_i-\mathbf{r}_{0,i})^2/\sigma^2+\sum_{i=1}^{N}\lambda[1-\cos(\theta_{i0})], \tag{10}$$

where $\mathbf{r}_i$ and $\mathbf{u}_i$ denote, respectively, the center-of-mass position and orientation of bowl i and $\mathbf{r}_{0,i}$ the lattice site of particle i, θ_{i0} is the angle between $\mathbf{u}_i$ and the ideal tilt vector of particle i, and $\beta=1/k_BT$. The Helmholtz free energy [34] of the noninteracting Einstein crystal is modified accordingly, but the only modification is the integral over the angular coordinates,

$$J(\lambda)=\int_{-1}^{1}e^{\lambda(x-1)}dx=\frac{1-e^{-2\lambda}}{\lambda}. \tag{11}$$

Although the shape of the bowls is more complex than that of the dumbbell, we can still use a rather simple form for the pairwise soft potential interaction,

$$\beta U_{\text{soft}}(\mathbf{r}^N,\mathbf{u}^N;\gamma)=\sum_{i<j}\beta\varphi(\mathbf{r}_i-\mathbf{r}_j,\mathbf{u}_i,\mathbf{u}_j,\gamma) \tag{12}$$

with

$$\beta\varphi(\mathbf{r}_j-\mathbf{r}_i,\mathbf{u}_i,\mathbf{u}_j,\gamma) = \begin{cases} \gamma(1-A(r'_{ij}/\sigma_{\max})^2) & \text{if } i \text{ and } j \text{ overlap} \\ 0 & \text{otherwise} \end{cases}, \tag{13}$$

where $r'_{ij}\equiv|\mathbf{r}_j-\mathbf{r}_i+\frac{\sigma-D}{2}(\mathbf{u}_i-\mathbf{u}_j)|$ i.e., the distance between the "centers" of bowl i and bowl j, $\sigma_{\max}$ is the maximal r'_{ij} for which the particles overlap: $\sigma_{\max}^2=\sigma^2+(\sigma-D)^2$, A is an adjustable parameter that is kept fixed during the simulation at a value $A=0.5$, and γ is the integration parameter. It was shown in Ref. [35] that in order to minimize the error and maximize the efficiency of the free energy calculation, the potential must decrease as a function of r and must exhibit a discontinuity at r such that both the amount of overlap and the number of overlaps decrease upon increasing γ. Here, we have chosen this particular form of the potential because it can be evaluated very efficiently in a simulation, although it does not describe the amount of overlap between bowls i and j very accurately. We checked that adding a term that tries to describe the angular behavior of the amount of overlap does not significantly change our results of the free energy calculations. Also, we checked that by employing the usual Einstein integration method (i.e., only hard-core interactions) at a relatively low density we obtained the same result as by using the method of Fortini *et al.* [35]. Finally, we set the maximum interaction strength $\gamma_{\max}$ to 200.

We perform variable box shape *NPT* simulations [29,30] to obtain the equation of state for varying D. In these simulations not only the edge length changes, but also the angles between the edges are allowed to change. We employ the averaged configurations in the Einstein crystal thermodynamic integration. We calculate the free energy as a function of density by integrating the EOS from a reference density to the density of interest,

$$F(\rho_1^*) = F(\rho_0) + \int_{\rho_0}^{\rho_1} d\rho \left\langle \frac{NP(\rho)}{\rho^2} \right\rangle. \tag{14}$$

III. RESULTS

A. Stacks

We perform standard Monte Carlo simulations in the isobaric-isothermal ensemble (*NPT*). Figure 2 shows a typical configuration of bowl-shaped particles with $D=0.3\sigma$ at $P\sigma^3/k_BT=50$, displaying stacking behavior typical for the wormlike phase. The equation of state (EOS) of the fluid is somewhat peculiar: the pressure as a function of density is not always convex for all densities, although the compressibility does decrease monotonically with packing fraction ϕ for $D=0.1\sigma$, see Fig. 3, where the packing fraction is defined as $\phi=\frac{\pi D}{4}(\sigma^2-D\sigma+\frac{2}{3}D^2)N/V$. This behavior persist for all $D\leq 0.2\sigma$, but for $D\geq 0.25\sigma$ the pressure is always convex. We investigate the origin of these peculiarities using $g_c(z)$, the positional correlation function along the director of a particle, which includes only the particles in a column around a particle, as defined in Eq. (3). As can be seen from $g_c(z)$ in Fig. 4, the structure of the fluid changes dramatically as the pressure is increased. At $P^*\equiv\beta P\sigma^3=1$, the correlation function is typical for a low-density isotropic fluid of hemispherical particles; no effect of the dent of the particles is found at low densities. The only peculiar feature of $g_c(z)$ for $P^*=1$ is that it is not symmetric around zero, but this is caused by our choice of reference point on the particle [see Fig. 1(b)], which is located below the particle if the particle points upward. In contrast, at $P^*=10$ $g_c(z)$ already shows strong structural correlations. Most noteworthy is the peak at $z=D$, that shows that the fluid is forming short stacks of aligned particles. Also, note that the value of $g_c(z)$ is nonzero around $z=0$. This is caused by pairs of bowls that align antiparallel and form a spherelike object, as depicted in Fig. 4. Finally, at $P^*=50$ and higher, long wormlike stacks are fully formed and $g_c(z)$ shows multiple peaks at $z=Dn$ for both positive and negative integer values of n. Furthermore, at these pressures, there are no spherelike pairs, as can be observed from the value of $g_c(0)$. The formation of stacks explains the peculiar behavior of the pressure: At low densities,

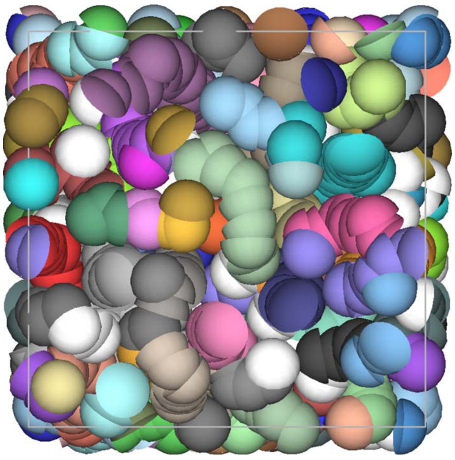

FIG. 2. (Color online) The final configuration obtained from simulations at $P\sigma^3/k_BT=50$ and $D=0.3\sigma$ The gray values (colors) denote different stacks.

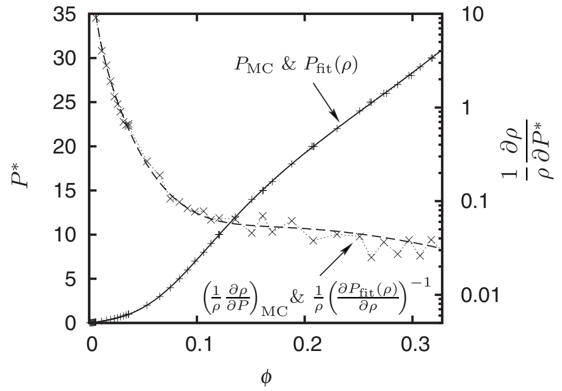

FIG. 3. The equation of state for bowl-shape particles with $D=0.1\sigma$, reduced pressure $P^*=\beta P\sigma^3$ (left axis), and the reduced compressibility $\frac{1}{\rho}\frac{\partial\rho}{\partial P^*}$ on a log scale (right axis) as a function of packing fraction ϕ. The points are data obtained from *NPT* simulations. The solid line is a fit $P_{\mathrm{fit}}(\rho)$ to the pressure; the dashed line is the corresponding reduced compressibility, $\frac{1}{\rho}(\frac{\partial P_{\mathrm{fit}}(\rho)}{\partial\rho})^{-1}$.

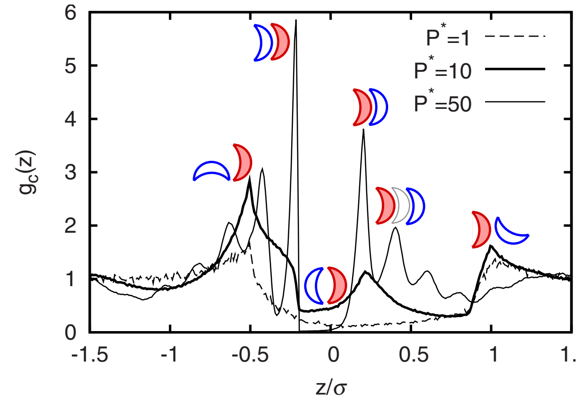

FIG. 4. (Color online) The pair correlation function, $g_c(z)$, of a fluid of bowl-shaped particles with $D=0.2\sigma$ as a function of the dimensionless interparticle distance z/σ along the axis of a reference bowl for various reduced pressures $P^* \equiv \beta P\sigma^3$. Only particles within a cylinder of diameter σ around the bowl are considered, as indicated by the subscript 'c'. We show typical two-particle configurations that contribute to $g_c(z)$ for $z/\sigma=-0.5$, -0.2, 0.2, 0.4, and 1, where the filled (red) bowl denotes the reference particle, and the open (blue) bowl with thick outlines denotes the other particle.

the bowls rotate freely, which means that the pressure will be dominated by the rotationally averaged excluded volume. The excluded volume of two particles that are not aligned is nonzero, even for $D=0$, and gives rise to the convex pressure which is typical for repulsive particles. As the density increases and the bowls start to form stacks, the available volume increases, and the pressure increases less than expected, which can even cause the EOS to be concave. At even higher densities the wormlike stacks are fully formed, and the pressure is again a convex function of density for $D>0$, dominated by the excluded volume of locally aligned bowls. The excluded volume of completely aligned infinitely thin bowls is zero, and, therefore, the pressure increases almost linearly with density for $D=0$ when the stacks are fully formed.

To quantify the length of the stacks we calculated the stack distribution as shown in Fig. 5. As can be seen from the figure, the length of the stacks is strongly dependent on D/σ. However, we have found that above a certain threshold pressure the distribution of stacks is nearly independent of pressure.

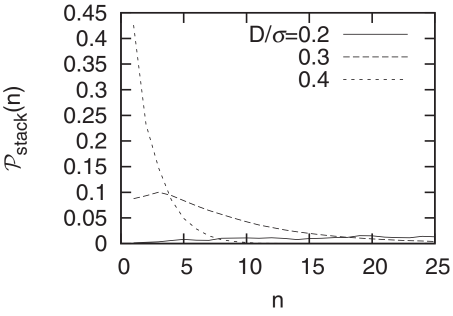

FIG. 5. The probability, $\mathcal{P}_{\rm stack}(n)$, to find a particle in a stack of size n for $D/\sigma=0.2$, 0.3, and 0.4 and $P\sigma^3/k_BT=50$

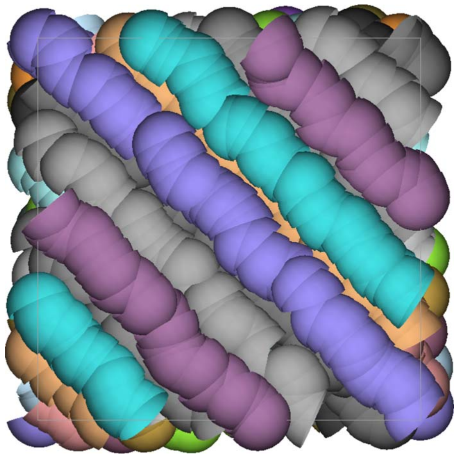

FIG. 6. (Color online) The final configuration of a simulation of bowls with $L=0.1D$ at $P\sigma^3/k_BT=38$. The gray values (colors) denote different columns.

We investigated whether the wormlike stacks could spontaneously reorient to form a columnar phase. We increased the pressure in small steps of 1 k_BT/σ^3 from well below the fluid-columnar transition to very high pressures, where the system was essentially jammed. At each pressure, we ran the simulation for 4×10^6 Monte Carlo cycles, where a cycle consists of N particle and volume moves. These simulations show that the bowls with a thickness $D \geq 0.25\sigma$ always remained arrested in the wormlike phase, which is similar to the experimental observations [22]. However, for $D/\sigma=0.1$ and 0.2, we find that the system eventually transforms into a columnar phase in the simulations (see Fig. 6). This might be explained by the fact that the isotropic-to-columnar transition occurs at lower packing fractions for deeper bowls (smaller D), which facilitates the rearrangements of the particles into stacks and the alignment of the stacks into the columnar phase.

B. Packing

We found six candidate crystal structures, denoted X, IX, IX′, B, IB, and fcc², using the pressure annealing method. Snapshots of a few unit cells of these crystal phases are shown in Fig. 7. We will describe these crystal structures using the order parameters S_1, that measures alignment of the particles, and the nematic order parameter (S_2), that is nonzero for both parallel and antiparallel configurations. Crystal structure X has $S_1 \simeq 1$ and $S_2 \simeq 1$, and the particles are stacked head to toe in columns. The lattice vectors are

$$\mathbf{a_1} = \sigma\hat{x} \quad \mathbf{a_2} = D\hat{z},$$

$$\mathbf{a_3} = \frac{\sigma}{2}\hat{x} + \frac{1}{2}\sqrt{\sigma^2 - D^2 + 2\sigma\sqrt{\sigma^2 - D^2}}\hat{y} + \frac{D}{2}\hat{z}, \tag{15}$$

and the density is

$$\rho\sigma^3 = \left[\frac{D\sigma}{2}\sqrt{\sigma^2 - D^2 + 2\sigma\sqrt{\sigma^2 - D^2}}\right]^{-1}. \tag{16}$$

The order parameters of the second crystal structure, are $S_1 \simeq 0$ and $S_2 \simeq 1$, which is caused by the fact that half of the

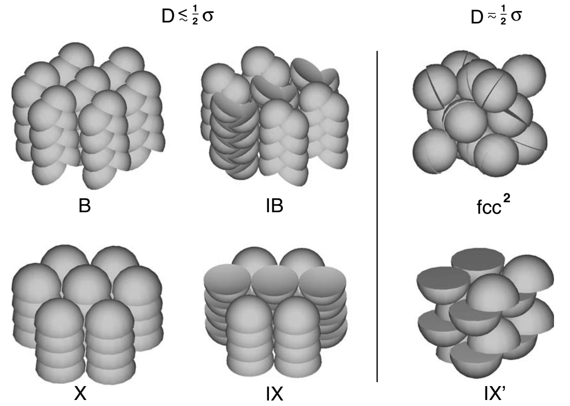

FIG. 7. The various crystal phases that were considered as possible stable structures. Five of these were found using the pressure annealing method: X, IX, B, IB and IX′. X, IX, B, and IB are densely packed structures for $D \lesssim 0.5\sigma$ and fcc^2 and IX′ are densely packed crystal structures for (nearly) hemispherical bowls ($D \simeq 0.5\sigma$).

particles point upward, and the other half downward. Further investigation shows that there are two phases with $S_2 \simeq 1$ and $S_1 \simeq 0$: one at low D (IX) and one at $D \simeq \sigma/2$ (IX′). The structure within the columns of the first (IX) of these two structures is the same as for the X structure, but one half of these columns are upside down, like in the inverted columnar phase (in fact, the IX crystal melts into the inverted columnar phase). The lattice vectors of crystal structure IX are

$$\mathbf{a_1} = \sigma\hat{x} \quad \mathbf{a_2} = D\hat{z}$$

$$\mathbf{a_3} = \frac{\sigma}{2}\hat{x} + \frac{1}{2}\sqrt{3\sigma^2 - 4D^2}\hat{y}, \tag{17}$$

and the density is

$$\rho\sigma^3 = \left[\frac{D\sigma}{2}\sqrt{3\sigma^2 - 4D^2}\right]^{-1}. \tag{18}$$

The columns in the IX crystal are arranged in such a way that the rims of the bowls can interdigitate. The IX′ crystal can be obtained from the IX phase at $D=\sigma/2$ by shifting every other layer by some distance perpendicular to the columns, such that the particles in these layers fit into the gaps in the layers below or above. In this way a higher density than Eq. (18) is achieved. The columns of the third crystal phase (B) resemble braids with alternating tilt direction of the particles within each column. Because of this tilt S_1 and S_2 have values between 0 and 1, that depend on D. Furthermore, the inverted braids structure (IB), that has $0 < S_2 < 1$ and $S_1 = 0$, can be obtained by flipping one half of the columns of the braidlike phase (B) upside down. These braidlike columns piece together in such a way that the particles are interdigitated. In other words, this phase is related to the B phase in exactly the same way as the IX phase is related to the X phase. Finally, in the paired face-centered-cubic (fcc^2) phase, pairs of hemispheres form spherelike objects that can rotate freely and that are located at the lattice positions of an fcc crystal. The density at close packing is $2\sqrt{2}/\sigma^3$, i.e., twice the density of fcc.

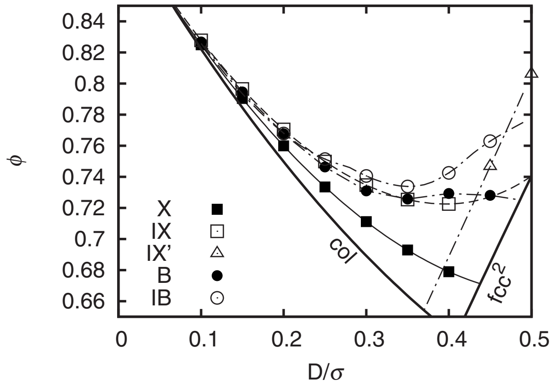

FIG. 8. Packing diagram: maximum packing fraction (ϕ) of various crystal phases as a function of the thickness (D) of the bowls. The points are the results of the pressure annealing simulations. The thin dot-dashed lines are obtained from the pressure annealing results by slowly increasing or decreasing D as described in Sec. II D, except for the IX phase (thin dashed line with open squares) and the X phase (thin solid line with filled squares), for which the packing fraction can be expressed analytically. The thick lines denote the packing fractions of the perfect hexagonal columnar phase (col) and the paired fcc phase (fcc^2). Any points that lie below these lines are expected to be thermodynamically unstable (see text).

In Fig. 8 the results of the pressure annealing method are shown, along with the known packing fraction of the perfect hexagonal columnar phase (col). Since the columnar phase has positional degrees of freedom and the fcc^2 phase has rotational degrees of freedom, we expect these phases to have a higher entropy (lower free energy) than any crystal phase with the same or lower maximum packing fraction whose degrees of freedom have all been frozen out. Therefore, any crystal structure with a packing fraction below the thick lines in Fig. 8 is most likely thermodynamically unstable. At first, we were unable to find the fcc^2 using the pressure annealing method as described in Sec. II D. However, if we increase the pressure slowly to $100k_BT/\sigma^3$ in simulations of 12 particles, we did observe the fcc^2 phase for hemispherical particles ($D=\sigma/2$). In these simulations at finite pressure, it is important to constrain the length of all box vectors such that they remain larger than say 1.5σ. Otherwise the box will become extremely elongated, such that the particles can interact primarily with their own images. When a particle interacts with it is neighbors, the Gibbs free energy $G=F+PV$ decreases, because the volume decreases without any decrease in entropy due to restricted translational motion (if a particle moves, its image moves as well, so a particle translation will never cause overlap of the particle with its image). The decrease in Gibbs free energy is of course an extreme finite size effect, which should be avoided if we wish to predict the equilibrium phase behavior. For the pressure annealing simulations at very high pressures, these effects are not important, because the entropy term in the Gibbs free energy is small compared to PV. We did not attempt to find the columnar phase using the modified pressure annealing method, as we were only interested in finding can-

TABLE I. Free energy differences, $f_{\mathrm{diff}} \equiv [F_{\mathrm{col}}(\rho_{\mathrm{col}}) - F_{\mathrm{fluid}}(\rho_{\mathrm{fluid}})]/(Nk_BT)$, between the (inverted) columnar phase at density ρ_{col} or packing fraction ϕ_{col} and the fluid phase at ρ_{fluid} or ϕ_{fluid}. In the column "phases," "col" denotes the columnar phase and inverted columnar phase is abbreviated to "inv col."

Phases	D/σ	$\rho_{\mathrm{fluid}}\sigma^3$	$\rho_{\mathrm{col}}\sigma^3$	f_{diff}
fluid–col	0	1.461	4.679	7.33272
Phases	D/σ	ϕ_{fluid}	ϕ_{col}	f_{diff}
fluid–col	0.1	0.1780	0.2848	3.2630(7)
fluid–col	0.2	0.3116	0.4674	3.268(2)
fluid–col	0.3	0.3760	0.5193	3.802(1)
fluid–inv col	0.3	0.3760	0.5193	3.8155(8)
fluid–col	0.4	0.4440	0.5772	5.843

didate crystal structures. Furthermore, the columnar phase was already found in more standard simulations with a larger number of particles.

C. Free energies

In order to determine the regions of the stability of the fluid, the columnar phase and the six crystal phases, we calculated the free energies of all phases as explained in the Methods section. The results of the reference free energy calculations are shown in Tables I and II.

We find that the columnar phase with all the particles pointing in the same direction is more stable than the inverted columnar phase, where half of the columns are upside down. However, the free energy difference between the two phases is only $0.013 \pm 0.002 k_BT$ per particle at $\phi = 0.5193$ and $D = 0.3\sigma$. Based on this small free energy difference we do not expect polar ordering to occur spontaneously. Similar conclusions, based on direct simulations, were already drawn in Ref. [2].

The densely packed crystal structures in Fig. 7 at $D \lesssim 0.3$, the wormlike fluid phase (Fig. 2) and the columnar phase (Fig. 6) show striking similarity in the local structure: in all these phases the bowls are stacked on top of each other, such that (part of) one bowl fits into the dent of another bowl. As a result, the free energies and pressures of the various phases, are often almost indistinguishable near coexistence. For this reason it was sometimes difficult to determine the coexistence densities for $D < 0.3\sigma$. Exemplary free energy curves for the various stable phases consisting of bowls with $D = 0.3\sigma$ are shown in Fig. 9.

TABLE II. Excess free energies, $f_{\mathrm{exc}} \equiv (F - F_{\mathrm{id}})/(Nk_BT)$, of the various crystal phases, where F_{id} is the ideal gas free energy. The various crystal phases are labeled as in Fig. 7.

Phase	D/σ	ϕ	f_{exc}
IX	0.3	0.6669	15.505(4)
IB	0.3	0.6971	18.407(3)
IX	0.4	0.6177	12.52(1)
IB	0.4	0.6170	13.195(2)
IX	0.45	0.6768	17.918(2)
IB	0.45	0.6662	14.9873(4)
fcc^2	0.45	0.6192	12.8591(5)
IX′	0.45	0.6950	18.170(5)
fcc^2	0.5	0.5455	8.7673(7)
IX′	0.5	0.5597	10.854(3)

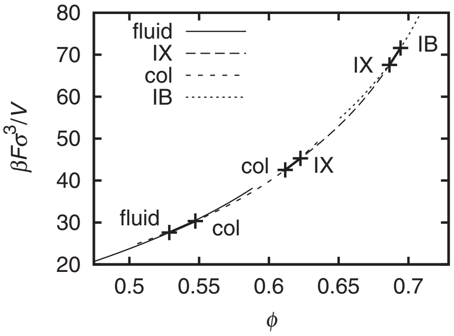

FIG. 9. Dimensionless free energies $\beta F\sigma^3/V$ for hard bowls with $L = 0.3\sigma$ and the fluid-columnar, columnar-IX and IX-IB coexistences, which were calculated using common tangent constructions. The columnar phases is denoted "col." The irrelevant free energy offset is defined in such a way that the free energy of the ideal gas reads $\beta F/V = \rho[\log(\rho\sigma^3) - 1]$. The free energies of the various phases are so close, that they are almost indistinguishable.

D. Phase diagram

In Fig. 10, we show the phase diagram in the packing fraction ϕ-thickness D/σ representation. The packing frac-

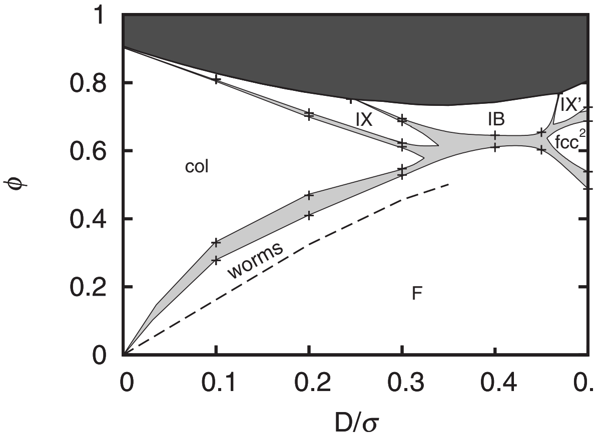

FIG. 10. Phase diagram in the packing fraction (ϕ) versus thickness (D) representation. The light gray areas are coexistence areas, while the state points in the dark gray area are inaccessible since they lie above the close packing line. IX, IB, IX′ and fcc^2 denote the crystals as shown in Fig. 7, "F" is the fluid and "col" is the columnar phase. The lines are a guide to the eyes. Wormlike stacks were found in the area marked "worms" bounded from below by the dashed line. This line denotes the probability to find a particle in a cluster that consists of more than two particles, $\mathcal{P}_{\mathrm{stack}}(n > 2) = 1/2$.

TABLE III. Reduced densities, pressures, and chemical potentials $\mu^*=\beta\mu-\ln(\Lambda_t^3\Lambda_r/\sigma^3)$ of the coexisting phases for hard bowl-shaped particles with thickness D.

D/σ	Phase 1	Phase 2	$\rho_1\sigma^3$	$\rho_2\sigma^3$	$\beta P\sigma^3$	μ^*
0	fluid	col	4.083	4.824	26.11	15.22

D/σ	Phase 1	Phase 2	ϕ_1	ϕ_2	βPd^3	μ^*
0.1	fluid	col	0.2778	0.3297	26.35	15.59
0.1	col	IX	0.8095	0.8104	2.7×10^3	
0.2	fluid	col	0.4096	0.4688	27.23	16.68
0.2	col	IX	0.7021	0.7108	325	
0.3	fluid	col	0.5286	0.5472	49.52	26.13
0.3	col	IX	0.6864	0.6944	281.4	91.03
0.3	IX	IB	0.6117	0.6226	110.9	44.92
0.4	fluid	IB	0.6098	0.6455	105.9	51.06
0.45	fluid	IB	0.6026	0.6545	87.92	46.90
0.5	fluid	fcc^2	0.4878	0.5383	28.34	22.10
0.5	fcc^2	IX$'$	0.6870	0.7278	139.2	67.36

tion is defined as $\phi=\frac{\pi D}{4}(\sigma^2-D\sigma+\frac{2}{3}D^2)N/V$. For $D/\sigma\leq0.3$, we find an isotropic-to-columnar phase transition at intermediate densities, which resembles the phase diagram of thin hard disks [24]. However, the fluid-columnar-crystal triple point for disks is at a thickness-to-diameter ratio of about $L/\sigma\sim0.2-0.3$, while in our case the triple point is at about $D/\sigma\sim0.3-0.4$. The shape of the bowls stabilizes the columnar phase compared to the fluid and the crystal phase. We find four stable crystal phases IX, IB, IX$'$, and fcc^2, while we had six candidate crystals. The two phases that were not stable are the X and B crystals, which are very similar to the stable IX and IB crystals respectively, except that X and B have considerable lower close packing densities. Therefore, one could have expected these phases to be unstable. On the other hand, we observe from the phase diagram, that IX is stable at intermediate densities for $0.25\sigma<D<0.45\sigma$, while IB packs better than IX. In other words, stability cannot be inferred from small differences in packing densities.

Almost all coexistence densities were calculated by employing the common tangent construction to the free energy curves, except for the col–IX coexistence at $D=0.1\sigma$ and 0.2σ. At these values of D the transition occurs at very high pressures, while the free energy of the columnar phase is calculated at the fluid–col transition, which occurs at a low pressure. To get a value for the free energy of the columnar phase we would have to integrate the equation of state up to these high pressures, accumulating integration errors. Furthermore, we expect the coexistence to be rather thin, which would further complicate the calculation. So, instead we just ran long variable box shape *NPT* simulations to see at which pressure the IX phase melts into the inverted columnar phase. As the free energy difference between the inverted columnar phase and the columnar phase is small, we assume that this is the coexistence pressure for the col–IX transition, although technically it is only a lower bound. The density of the columnar phase at this pressure is determined using a local fit of the equation of state. All coexistences are tabulated in Table III. We draw a tentative line in the phase diagram to mark the transition from a structureless fluid to a wormlike fluid i.e., a fluid with many stacks. In a dense but structureless fluid, stacks of size 2 are quite probable, but larger stacks occur far less frequently. We calculate the probability to find a particle in a stack that contains more than 2 particles $\mathcal{P}_{\text{stack}}(n>2)=1-\mathcal{P}_{\text{stack}}(1)-\mathcal{P}_{\text{stack}}(2)$ and define the wormlike phase by the criterion $\mathcal{P}_{\text{stack}}(n>2)\geq1/2$ in Fig. 10. We do not imply that the transition to the wormlike phase is a true thermodynamic phase transition; the transition is rather continuous. The type of stacks in the fluid changes from wormlike for $D=0.3\sigma$ to something resembling the columns in the braidlike crystals B and IB (see Fig. 7) for $D=0.4\sigma$. Therefore, the region of stability wormlike phase was ended at $D=0.35\sigma$, where there are similar amounts of braidlike and wormlike stacks.

IV. SUMMARY AND DISCUSSION

We have studied the phase behavior of hard bowls in Monte Carlo simulations. We find that the bowls have a strong tendency to form stacks, but the stacks are bent and not aligned. We measured the equation of state and the compressibility in Monte Carlo *NPT* simulations. The pressure we obtained from these simulations is concave for some range of densities for deep bowls. This is due to the increase in free volume when large stacks form. Using $g_c(z)$, the pair correlation function along the direction vector, we showed that the concavity of the pressure coincides with a dramatic change in structure from a homogeneous fluid to the wormlike fluid. We measured the three-dimensional stack length distribution in the simulations. When the pressure is increased slowly, the deep bowls spontaneously order into a columnar phase in our simulations. This poses severe restrictions on the thickness of future bowl-like mesogens (molecular or colloidal), which are designed to easily order into a globally aligned lyotropic columnar phase. We determined the phase diagram using free energy calculations for a particle shape ranging from an infinitely thin bowl to a solid hemisphere. We find that the columnar phase is stable for $D \leq 0.3\sigma$ at intermediate packing fractions. In addition, we show using free energy calculations that the stable columnar phase possesses polar order. However, the free energy penalty for flipping columns upside down is very small, which makes it hard to achieve complete polar ordering in a spontaneously formed columnar phase of bowls.

ACKNOWLEDGMENTS

We thank Rob Kortschot, Ahmet Demirörs and Arnout Imhof for useful discussions. Financial support is acknowledged from an NWO-VICI grant and from the High Potential Programme of Utrecht University.

APPENDIX: OVERLAP ALGORITHM

The overlap algorithm for our bowls checks whether the surfaces of two bowls intersect. Figure 1 shows that the surface of the bowl consists of two parts. Part p of the surface contains the part of the surface of the sphere of radius R_p, within an angle θ_p from the z axis, where $p=1$ denotes the smaller sphere and the larger sphere is labeled $p=2$. We set $\theta_1=\pi/2$, to get a hemispherical outer surface. The edges of both surfaces have to coincide, such that our particles have a closed surface. Using this restriction L, θ_2 and R_2 can all be expressed in terms of the radius of the smaller sphere, R_1, and the thickness of the bowl D, in the following way:

$$R_2 = R_1 + \frac{D^2}{2(R_1 - D)}, \tag{A1}$$

$$\theta_2 = \arcsin(R_1/R_2), \tag{A2}$$

$$L = R_2 \cos(\theta_2). \tag{A3}$$

Overlap occurs if either of the two parts of the surface of a bowl overlaps with either of the two parts of another bowl. So we have to check four pairs of infinitely thin (and not necessarily hemispherical) bowls, labeled i and j, for overlap. The algorithm for two such surfaces that are equal in shape was already implemented by He and Siders [36] as part of their overlap algorithm for their "UFO" particles, which are defined as the intersection between two spheres. An equivalent overlap algorithm was used by Cinacchi and Duijneveldt [12] to simulate infinitely thin contact lenselike particles, but the overlap algorithm was not described explicitly. We cannot use one of these algorithms, since the two parts of the surface of our particle are unequal in shape. Therefore, we implemented a slightly different version of the overlap algorithm, which we describe in the remainder of this section. In our overlap algorithm, the existence of an overlap or intersection between two infinitely thin bowls is checked in three steps.

(i) First, we check whether the full surfaces of the spheres intersect, i.e., $|R_i - R_j| < r_{ij} \equiv |\mathbf{r}_j - \mathbf{r}_i| < R_i + R_j$. If this intersection does not exist, there is no overlap, otherwise we proceed to the next step.

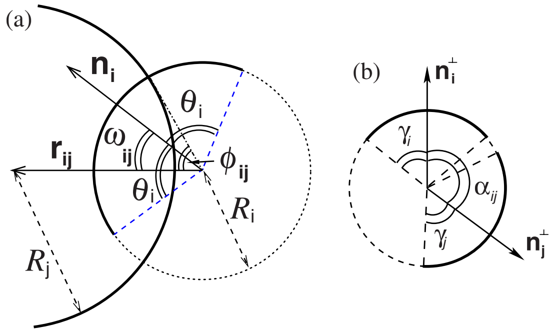

FIG. 11. (Color online) The relevant lengths and angles which are used in the first and second steps (a) and in the third step (b) of the overlap algorithm. Shown are bowl i and (part of) the sphere of bowl j (a), the arcs of i and j and the circular intersection of the spheres of i and j (b). In (a) $\mathbf{r}_{ij}$ lies in the plane, while the plane of view in (b) is perpendicular to $\mathbf{r}_{ij}$. In this case, the sphere of particle j overlaps with bowl i, but the arcs do not overlap, so particle i and particle j do not overlap.

(ii) Second, we determine the intersection of the surface of each sphere with the other bowl. The intersection of bowl i with the sphere of bowl j exists if

$$|\omega_{ij} + \zeta\phi_{ij}| < \theta_i \tag{A4}$$

for $\zeta=1$ or -1, where

$$\cos(\phi_{ij}) = \frac{R_i^2 - R_j^2 + r_{ij}^2}{2 r_{ij} R_i} \quad \text{and} \tag{A5}$$

$$\cos(\omega_{ij}) = \frac{\mathbf{u}_i \cdot \mathbf{r}_{ij}}{r_{ij}}. \tag{A6}$$

see Fig. 11(a). This intersection is an arc, which is part of the circle that is the intersection between the two spheres. If in fact this arc is a full circle and the other particle has a nonzero intersection, the particles overlap. This is the case when Eq. (A4) holds for $\zeta=1$ *and* $\zeta=-1$. If, on the contrary, either of the two arcs does not exist, there is no overlap. Otherwise, if both arcs exist, but neither of them is a full circle, proceed to the next step.

(iii) Finally, if the two arcs overlap there is overlap, otherwise the particles do not overlap. The arcs overlap if

$$|\alpha_{ij}| < |\gamma_i| + |\gamma_j|, \tag{A7}$$

where

$$\cos(\alpha_{ij}) = \frac{\mathbf{n}_i^{\perp} \cdot \mathbf{n}_j^{\perp}}{|\mathbf{n}_i^{\perp}||\mathbf{n}_j^{\perp}|}, \tag{A8}$$

$$\cos(\gamma_i) = \frac{\cos(\theta_i) - \cos(\phi_{ij})\cos(\omega_{ij})}{\sin(\phi_{ij})\sin(\omega_{ij})}, \tag{A9}$$

where $\mathbf{n}_i^{\perp} = \mathbf{n}_i - (\mathbf{r}_{ij} \cdot \mathbf{n}_i)\mathbf{r}_{ij}/r_{ij}^2$ and the expressions for γ_j and $\mathbf{n}_j^{\perp}$ are equal to the expressions for γ_i and $\mathbf{n}_i^{\perp}$ with i and j interchanged. The arcs together with the relevant angles are drawn in Fig. 11(b).

The inequalities (A4) and (A7) are expressed in cosines and sines using some simple trigonometry. In this way no inverse cosines need to be calculated during the overlap algorithm.

For $D=0.5\sigma$ the bottom surface is a disk rather than an infinitely thin bowl. So the overlap check consists of bowl-bowl, bowl-disk and disk-disk overlap checks. For brevity, we will not write down the bowl-disk overlap algorithm, but it can be implemented in a similar way as the algorithm for bowl-bowl overlap described above. The disk-disk overlap algorithm was already implemented by Eppenga and Frenkel [37].

---

[1] K. M. Rabe, M. Dawber, C. Lichtensteiger, C. H. Ahn, and J.-M. Triscone, *Physics of Ferroelectrics* (Springer, Berlin; Heidelberg, 2007), pp. 1–30.

[2] M. Ricci, R. Berardi, and C. Zannoni, Soft Matter **4**, 2030 (2008).

[3] M. Sawamura, K. Kawai, Y. Matsuo, K. Kanie, T. Kato, and E. Nakamura, Nature (London) **419**, 702 (2002).

[4] C. D. Simpson, J. Wu, M. D. Watson, and K. Müllen, J. Mater. Chem. **14**, 494 (2004).

[5] B. Xu and T. M. Swager, J. Am. Chem. Soc. **115**, 1159 (1993).

[6] J. Malthete and A. Collet, J. Am. Chem. Soc. **109**, 7544 (1987).

[7] P. W. Rabideau and A. Sygula, Acc. Chem. Res. **29**, 235 (1996).

[8] D. M. Forkey, S. Attar, B. C. Noll, R. Koerner, M. M. Olmstead, and A. L. Balch, J. Am. Chem. Soc. **119**, 5766 (1997).

[9] Y. Matsuo, K. Tahara, M. Sawamura, and E. Nakamura, J. Am. Chem. Soc. **126**, 8725 (2004).

[10] H. Sakurai, T. Daiko, H. Sakane, T. Amaya, and T. Hirao, J. Am. Chem. Soc. **127**, 11580 (2005).

[11] T. Kawase and H. Kurata, Chem. Rev. **106**, 5250 (2006).

[12] G. Cinacchi and J. S. van Duijneveldt, J. Phys. Chem. Lett. **1**, 787 (2010).

[13] C. I. Zoldesi, C. A. van Walree, and A. Imhof, Langmuir **22**, 4343 (2006).

[14] C. Charnay, A. Lee, S.-Q. Man, C. E. Moran, C. Radloff, R. K. Bradley, and N. J. Halas, J. Phys. Chem. B **107**, 7327 (2003).

[15] X. D. Wang, E. Graugnard, J. S. King, Z. L. Wang, and C. J. Summers, Nano Lett. **4**, 2223 (2004).

[16] J. Liu, A. I. Maaroof, L. Wieczorek, and M. B. Cortie, Adv. Mater. (Weinheim, Ger.) **17**, 1276 (2005).

[17] D. Jagadeesan, U. Mansoori, P. Mandal, A. Sundaresan, and M. Eswaramoorthy, Angew. Chem. Int. Ed. **47**, 7685 (2008).

[18] J. C. Love, B. D. Gates, D. B. Wolfe, K. E. Paul, and G. M. Whitesides, Nano Lett. **2**, 891 (2002).

[19] I. D. Hosein and C. M. Liddell, Langmuir **23**, 8810 (2007).

[20] T. Higuchi, H. Yabu, and M. Shimomura, Colloids Surf., A **284-285**, 250 (2006).

[21] Y. Lu, Y. Yin, and Y. Xia, Adv. Mater. (Weinheim, Ger.) **13**, 34 (2001).

[22] M. Marechal, R. J. Kortschot, A. F. Demirörs, A. Imhof, and M. Dijkstra, Nano Lett. **10**, 1907 (2010).

[23] B. Widom, J. Chem. Phys. **39**, 2808 (1963).

[24] J. A. C. Veerman and D. Frenkel, Phys. Rev. A **45**, 5632 (1992).

[25] M. A. Bates and D. Frenkel, Phys. Rev. E **57**, 4824 (1998).

[26] L. Filion, M. Marechal, B. van Oorschot, D. Pelt, F. Smallenburg, and M. Dijkstra, Phys. Rev. Lett. **103**, 188302 (2009).

[27] H. R. Karfunkel and R. J. Gdanitzt, J. Comput. Chem. **13**, 1171 (1992).

[28] A. P. Malanoski and P. A. Monson, J. Chem. Phys. **110**, 664 (1999).

[29] M. Parrinello and A. Rahman, Phys. Rev. Lett. **45**, 1196 (1980).

[30] R. Najafabadi and S. Yip, Scr. Metall. **17**, 1199 (1983).

[31] S. Torquato and Y. Jiao, Nature (London) **460**, 876 (2009).

[32] V. Buch, R. Martoňák, and M. Parrinello, J. Chem. Phys. **124**, 204705 (2006).

[33] D. Frenkel and B. Smit, *Understanding Molecular Simulation* (Academic, New York, 2002).

[34] M. Marechal and M. Dijkstra, Phys. Rev. E **77**, 061405 (2008).

[35] A. Fortini, M. Dijkstra, M. Schmidt, and P. P. F. Wessels, Phys. Rev. E **71**, 051403 (2005).

[36] M. He and P. Siders, J. Phys. Chem. **94**, 7280 (1990).

[37] R. Eppenga and D. Frenkel, Mol. Phys. **52**, 1303 (1984).